GEOPHYSICS

Frictional instabilities in clay illuminate the origin of slow earthquakes

Giuseppe Volpe[1]*, Cristiano Collettini[1,2], Jacopo Taddeucci[2], Chris Marone[1,3], Giacomo Pozzi[2]

The shallowest regions of subduction megathrusts mainly deform aseismically, but they can sporadically host slow-slip events (SSEs) and tsunami earthquakes, thus representing a severe hazard. However, the mechanisms behind these remain enigmatic because the frictional properties of shallow subduction zones, usually rich in clay, do not allow earthquake slip according to standard friction theory. We present experimental data showing that clay-rich faults with bulk rate-strengthening behavior and null healing rate, typically associated with aseismic creep, can contemporaneously creep and nucleate SSE. Our experiments document slow ruptures occurring within thin shear zones, driven by structural and stress heterogeneities of the experimental faults. We propose that bulk rate-strengthening frictional behavior promotes long-term aseismic creep, whereas localized frictional shear allows slow rupture nucleation and quasi-dynamic propagation typical of rate-weakening behavior. Our results provide additional understanding of fault friction and illustrate the complex behavior of clay-rich faults, providing an alternative paradigm for interpretation of the spectrum of fault slip including SSEs and tsunami earthquakes.

INTRODUCTION

Subduction zones accommodate deformation in a wide spectrum of fault slip motion: from aseismic creep, tremor, and slow earthquakes to regular earthquakes (*1*–*4*). Differently from regular earthquakes, which represent elasto-dynamic failure of locked faults, slow earthquakes represent quasi-dynamic fault slip transients along faults showing low interseismic coupling (*1*–*5*). Slow earthquakes have small stress drops, long rupture duration, and low rupture velocity producing seismic radiation depleted in high frequencies (*1*–*6*). Although slow earthquakes have been extensively studied on the deeper portion of subduction zones (depth < 50 km) (*3*, *4*, *7*), recent investigations reveal their occurrence along the shallowest portion of subduction zones (depth < 15 km) (*2*, *3*, *8*). Among shallow slow earthquakes, tsunami earthquakes (*9*) represent a severe hazard because they nucleate up-dip the seismogenic zone and propagate up to the trench generating unusually large tsunami for their magnitudes [moment magnitude (M_w) < 8] (*3*, *5*, *10*–*12*). Remarkable tsunami earthquakes include the 1947 Hikurangi event (*13*), the 1992 Nicaragua earthquake (*10*), the 1994 and 2006 Java earthquakes (*14*), and the 2010 Mentawai earthquake (*12*), many of which occurred in regions of low earthquake potential or seismic gaps (*3*, *12*, *14*). Moreover, catastrophic tsunamis are also generated by the up-dip continuation of great regular earthquakes producing large coseismic slip in the shallow portions of subduction zones [e.g., 2011 Tohoku-Oki; (*3*, *5*, *15*)]. The shallowest regions of subduction megathrusts often show low interseismic coupling (*5*, *8*, *16*–*18*), especially when unconsolidated clay-rich sediments are the most abundant rocks along the subduction interface (*19*, *20*). The low rigidity of the clay-rich sediments has been invoked to explain the anomalously slow rupture process of slow earthquakes (*3*, *10*, *11*, *21*). The low frictional strength, together with low healing rate of clay-rich rocks, assessed by laboratory experiments (*17*, *22*–*26*), supports the inferred frictional weakness and aseismic creep often observed along these clay-rich subduction interfaces (*5*, *8*, *16*–*18*). However, the dominant rate-strengthening behavior of clay-rich fault rocks cannot explain earthquake nucleation (*22*–*27*). In some laboratory experiments conducted on clay-rich fault rocks, a transition from rate-weakening to rate-strengthening frictional behavior with increasing loading velocities was observed (*27*) and invoked as a potential nucleation mechanism for slow-slip events (SSEs) (*8*). Recent works show that ultralow healing rates on weak faults influence nucleation and recurrence time of SSE (*17*). In addition, numerical models show that SSE can be produced along rate-strengthening faults by imposing temporal fluctuations of pore fluid pressure (*28*, *29*). While these observations suggest the possibility for earthquake nucleation within clay-rich faults, they do not provide a comprehensive characterization of the coexistence of SSE on experimental faults, which are continuously creeping during the interseismic phase. Therefore, the underlying processes are still elusive. Here, by integrating friction experiments, microstructural analysis, and an innovative video documentation of laboratory SSE, we provide an explanation for repetitive stick slip in rate-strengthening materials based on differences between bulk and local fault properties.

RESULTS

Mechanical and microstructural observations

To assess the seismogenic potential of materials relevant for the shallowest regions of subduction zones, we tested pure montmorillonite (fig. S1), a clay mineral abundant in several foredeep settings: e.g., Java, Costa Rica, Hikurangi, and Nankai (*19*, *20*). We performed experiments at room temperature, 100% relative humidity, and normal stresses (σ_N) ranging from 5 to 100 MPa using the double direct shear (DDS) setup (Fig. 1, Materials and Methods, and table S1). We measured shear strength (Fig. 1A), velocity dependence of friction (Fig. 1B), healing rate (fig. S2), and fault slip behavior at low forcing velocity (<0.1 μm/s; Fig. 1, C and D, and Materials and Methods). The velocity dependence of friction, expressed with the (*a*-*b*) parameter, defines the potential for unstable slip, while the healing rate is a measure of frictional strength recovery during times when faults are locked or slide slowly (*30*–*32*). In agreement with previous work (*22*), we found that montmorillonite obeys the Coulomb shear failure law at low normal stress, with a linear frictional envelope of μ =

[1]Dipartimento di Scienze della Terra, La Sapienza Università di Roma, Rome, Italy. [2]Istituto Nazionale di Geofisica e Vulcanologia, Rome, Italy. [3]Department of Geoscience, Pennsylvania State University, University Park, PA, USA.
*Corresponding author. Email: giuseppe.volpe@uniroma1.it

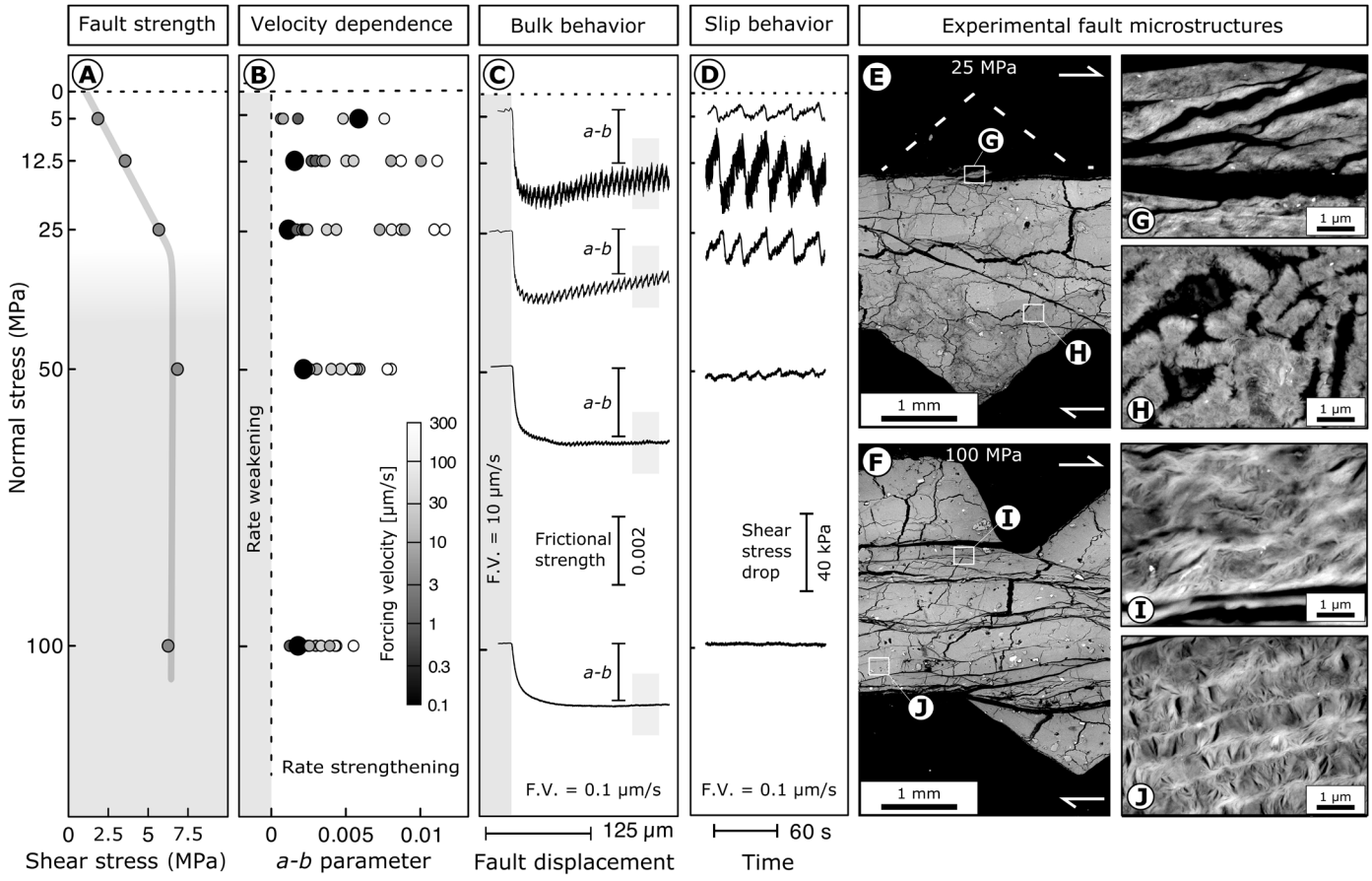

Fig. 1. Evolution of mechanical data and fault microstructures with normal stress. (**A**) Envelope of the steady-state shear stress showing a transition from frictional to ductile at $\sigma_N > 25$ MPa. (**B**) Rate-strengthening behavior (a-$b > 0$) is observed at all normal stresses (details in fig. S2 and table S2). (**C**) Shear stress evolution during a velocity step from 10 to 0.1 μm/s, showing a rate-strengthening trend. (**D**) Detail of the fault slip behavior showing stick-slip motion at low normal stress and forcing velocity (F.V.). (**E** and **F**) Fault microstructures of the experiments performed at 25 and 100 MPa, respectively (Materials and Methods). At low normal stress, where stick-slip instabilities occur, the microstructure shows a localized deformation zone <100 μm thick (**G** and **H**), whereas at higher normal stress the entire gouge volume is deformed exhibiting a well-developed foliation (**I** and **J**) and stable sliding [(C) and (D)]. The experiments reported in this figure are listed in table S1.

0.26 for $\sigma_N < 25$ MPa, whereas for $\sigma_N > 25$ MPa, the shear resistance of montmorillonite is constant (~6 MPa) and independent of normal stress, indicating a transition from frictional to ductile deformation (Fig. 1A), driven by frictional contact area saturation (*22*) and strain delocalization. We measured (a-b) during velocity-step tests from 0.1 to 300 μm/s and found rate-strengthening behavior with positive values of (a-b) (Fig. 1B, fig. S2, and table S2). At loading velocities of 0.1 μm/s, we observed SSE in the form of stick-slip motion with shear stress drops of tens of kilopascals (Fig. 1C). Normal stress and loading velocity control the emergence of slip instabilities; montmorillonite is unstable at normal stresses between 5 and 50 MPa (Fig. 1C) and forcing velocities <0.3 μm/s. The largest stress drops occurred at $\sigma_N = 12.5$ MPa, whereas at higher and lower σ_N, stress drops were smaller (Fig. 1C). The measured healing rates during slide-hold-slide test were zero for all normal stress tested (fig. S2). Overall, we document a transition from frictional to ductile rheology (Fig. 1A) with frictional properties indicating permanent fault weakness and continuous aseismic creep (Fig. 1B), punctuated by small instabilities (Fig. 1, C and D). The occurrence of frictional instabilities in rate-strengthening materials is of considerable interest and requires extensive analyses. Therefore, in the following, we first document fault fabric, characterizing frictional and ductile rheology, and then we explore the dynamics of such frictional instabilities. Microstructural analysis shows that experimental fault fabric changes as a function of normal stress (Fig. 1, E and F). At low normal stress, deformation is restricted to a thin zone (<100 μm) that develops parallel to the shear direction along one side of the fault (Fig. 1, E and G). The material in the shear zone is foliated (S-C fabric), with montmorillonite lamellae oriented favorably to the shear direction (Fig. 1G). Outside, the material appears undeformed, preserving the original vermicular shape of montmorillonite aggregates (Fig. 1H). At higher normal stresses, deformation is distributed and involves a thicker shear zone (fig. S3). At $\sigma_N = 100$ MPa, deformation pervades the whole sample, showing regular foliation (Fig. 1, F, I, and J).

Imaging instabilities

To explore the dynamics of frictional instabilities, we designed a method to directly observe sample deformation and fault slip, similarly to experiments performed in analog materials (*33*–*39*). Our experiment was performed using the same protocol and boundary conditions of experiments reported in Fig. 1 but using a transparent

(acrylic) slider block of the DDS setup (Fig. 2A). We imaged one side of the fault surface with reflected light during shear deformation. Videos were recorded using a high-speed, high-resolution digital camera, capturing the reflection of a light source on the fault-block interface (Fig. 2A and Materials and Methods). Changes in the intensity of reflected light, quantified by gray level [arbitrary units (a.u.)], correspond to changes in the local state of stress (see Materials and Methods), which can be detected at every point of the fault surface [Fig. 2B; (*36*, *40*, *41*)]. Our videos document a systematic, nonlinear, and inverse change of the average gray level as a function of the evolution of the shear stress (Fig. 2B and movies S1 to S18). We use the local evolution of the gray level as a proxy to monitor changes in the state of stress associated with rupture propagation, in a way similar to previous works that documented rupture propagation using strain gauges, digital image correlation, or local fault slip measurements (*37*–*39*). Each slip event corresponds to a systematic variation of the overall surface reflectivity (Fig. 2B), and the local variation of the surface reflectivity reveals the spatial-temporal evolution of the frictional instability (Fig. 2C and details in movies S1 to S18). We use a representative event to illustrate in detail the rupture process (Fig. 3). The substitution of the DDS slider block alters neither the bulk mechanical behavior nor the stick-slip instabilities; results for the acrylic and steel blocks are the same (fig. S4).

The rupture front can be tracked with the position of the first change in local reflectivity, corresponding to local change in the state of stress (white patches in Fig. 2C; colored lines in Fig. 3A). The rupture starts as a small patch that slowly (<3 mm/s) grows until it reaches a critical size of ~1 cm (Fig. 3A). During nucleation phase, as the patch widens (Fig. 3B), the local stress state decreases (Fig. 3C). After nucleation, the rupture front accelerates and propagates across the fault at an average velocity of ~15 cm/s (Fig. 3B). Behind the rupture front, the local state of stress first decreases to a minimum value and then gradually increases with time, indicating stress recovery (Fig. 3C). For a specific time window, the stress drop is restricted to the region between the rupture front and the onset of stress recovery (Fig. 3, D and E, and fig. S5). The region with a reduction in the stress state represents the breakdown zone of the propagating rupture (*42*). Our observations document rupture propagation along the fault in the form of self-healing wrinkle-like ruptures (*43*–*45*). In our experiments, nucleation sites are not related to pre-imposed asperities (*38*, *39*) but seem to be connected to spontaneous stress heterogeneities controlled by fault architecture (Riedel shears, Fig. 4) and, in a subordinate way, by stress redistribution following previous ruptures (fig. S6). These stress heterogeneities also modulate rupture velocity (Fig. 3B) and local stress drop (Fig. 3, C and D).

DISCUSSION

Slow-slip instabilities

Our laboratory experiments on clay-rich faults document a range of behaviors including low frictional strength, bulk rate-strengthening behavior, and null healing rate. We observe a transition from frictional to ductile rheology at σ_N > 25 MPa associated with a change

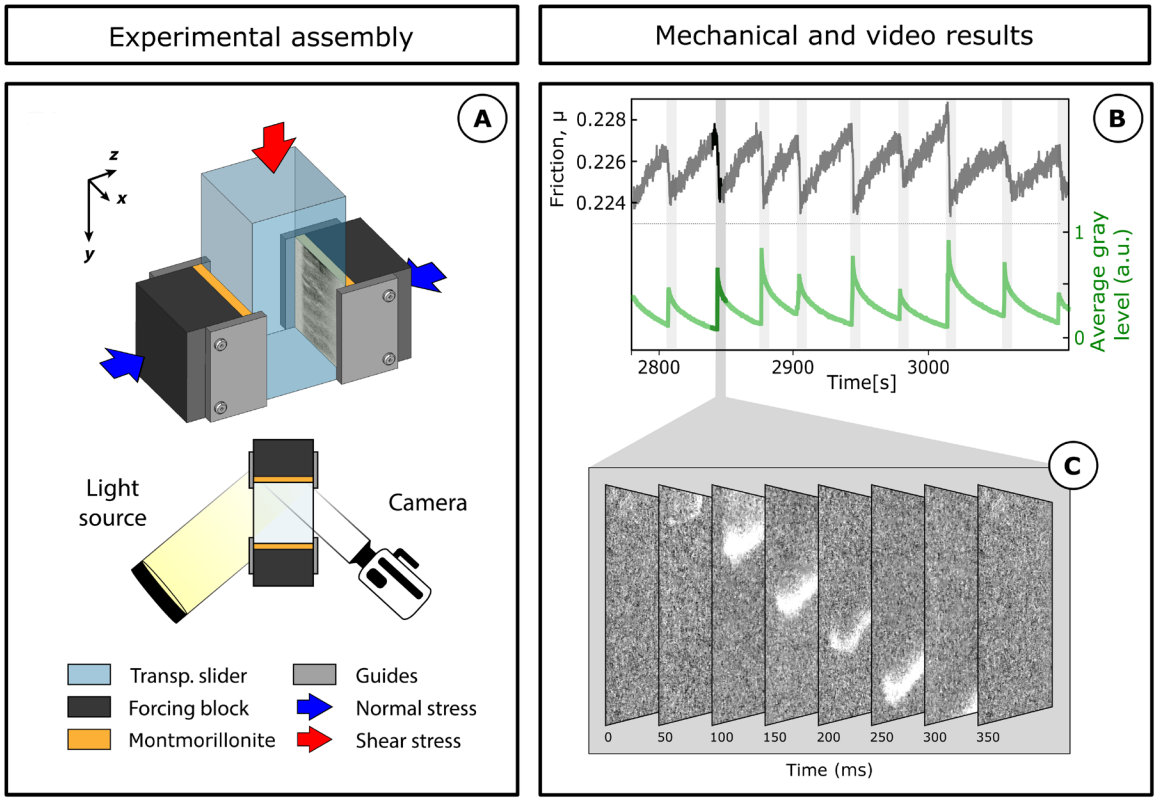

Fig. 2. Configuration and results of the video experiment. (**A**) Experimental design and assembly used for the video analysis of fault slip. (**B**) Comparison between mechanical data and bulk reflectivity changes (i.e., average gray level) showing an inverse, nonlinear relation between stress and reflectivity. (**C**) Frames of the video (movie S2) showing the spatial-temporal evolution of the rupture of the selected event (Materials and Methods). The data refer to experiment b1296 in table S1.

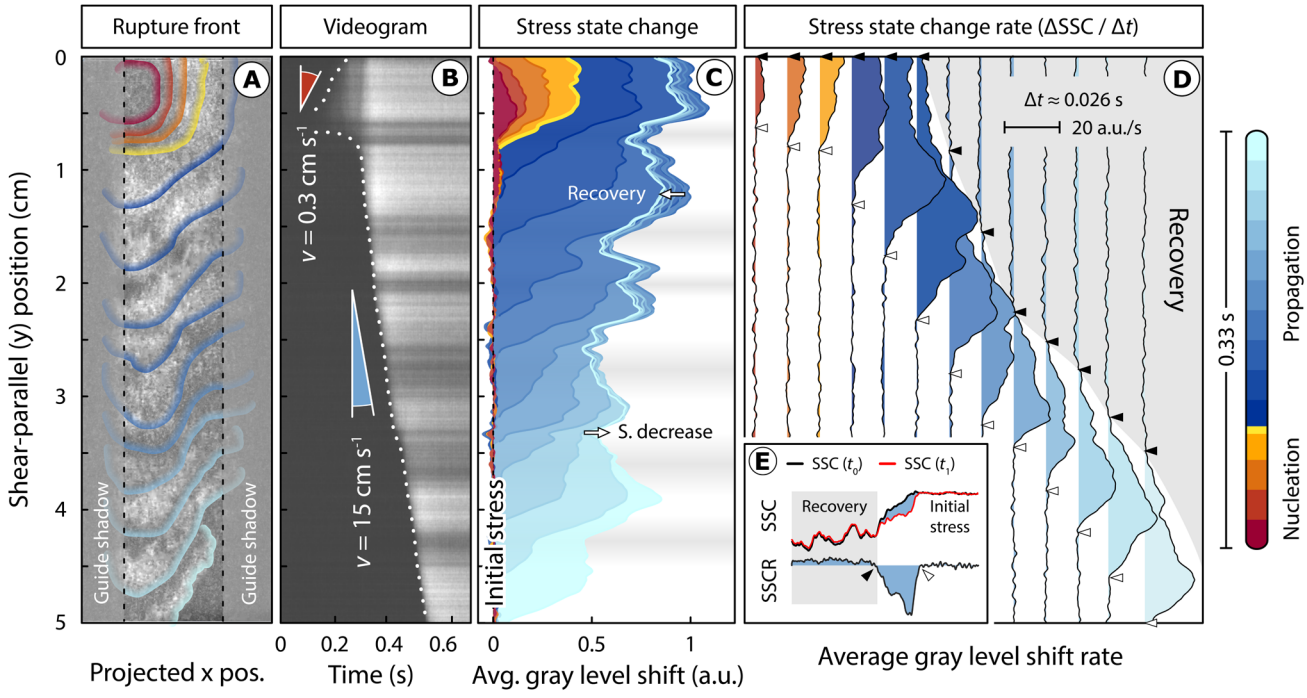

Fig. 3. Spatial-temporal evolution of the rupture properties of a single stick-slip event imaged from video analysis. (**A**) Space-time evolution of the rupture front on the fault surface. (**B**) Space-time position of the rupture front within the vertical dashed lines in (A). (**C**) Stress state change and (**D**) stress state change rate during time highlighted by changes in reflectivity (gray level, a.u.) proportional to the state of stress on fault (Materials and Methods and Fig. 8). (**E**) Description of the evolution of stress state change (SSC) and stress state change rate (SSCR) along the fault for a time window from t_0 to t_1 (details in fig. S5). The breakdown zone is restricted between the initial stress region (white arrow) and the recovery region (black arrow). Horizontal shades in (B) and (C) represent regions of the fault surface with stress heterogeneities caused by fault architecture (e.g., Riedel shear in Fig. 4).

from localized to distributed deformation (Fig. 1). These results agree with previous experimental works (*22*) using the rate-strengthening behavior of montmorillonite as justification for the observed aseismic creep of the shallowest regions of subduction zones (*5*, *8*, *12*). However, superimposed on the bulk rate-strengthening frictional rheology, we observe small slow-slip instabilities at low loading velocities (Figs. 1, C and D, and 4A). We interpret these instabilities as the result of second-order frictional mechanisms involving time-dependent adhesion (*40*, *41*, *46*) and structural-stress heterogeneities. Time-dependent adhesion promotes contact welding along the localized shear zone (Fig. 1E), similarly to frictional healing (*40*), and development of small fault patches acting as asperities and promoting nucleation (Figs. 1E, 3A, and 4B). To illuminate the role of adhesion, we have performed a specific experiment with the same protocol and boundary conditions at which we observed instabilities, but in this case, the montmorillonite is separated from the central forcing block by a thin layer of quartz particles (radius ~ 50 μm) (fig. S7). During this experiment, the absence of stick slip suggests that the presence of quartz particles along the fault surface reduces the efficiency of adhesive processes and inhibits frictional instabilities (*41*). Together with adhesion, our data show that structural and stress heterogeneities play a key role for the nucleation of instabilities. We observe that most of these instabilities systematically nucleate close to structural heterogeneities represented by the intersection between the fault surface and the Riedel shear planes (yellow lines in Fig. 4B). These structures divide the fault surface into elongated and subparallel domains along which the stress is not homogeneously distributed (Fig. 4B). Each fault domain shows a gradual transition from low stressed regions (white) to more stressed regions (black), whereas the transition is more abrupt across the Riedel shears (Fig. 4B). Most of the ruptures nucleate in regions with a relatively low state of stress (lighter colors in Fig. 4B and fig. S6), suggesting a key role of low stresses in favoring local changes of the frictional properties (*27*, *47*), hence favoring the nucleation of the observed slow-slip instabilities.

For the observed slow-slip instabilities, our data and images of the rupture process (Fig. 3) point to self-healing wrinkle-like ruptures (*43*–*45*). Similar rupture dynamics have been documented on bare-rock surfaces (*48*–*50*), plastic materials (*33*–*36*), or thin quartz powder layer (*37*–*39*). These experiments documented dynamic stress drops up to few megapascals and rupture velocity up to kilometers per second in rate-weakening faults. Our experiments extend these works to faults with bulk rate-strengthening behavior that also include repetitive stick-slip instabilities with small stress drops, slip, and rupture velocity. We connect these differences to the low rigidity, bulk rate-strengthening behavior, and null healing rate of montmorillonite, which limits the stress drop magnitude and the rupture velocity (*5*, *17*).

Implication for shallow SSE and tsunami earthquakes

Although dimensions and rupture velocities of natural and laboratory faults differ notably, and more comprehensive discussions are required, the striking similarities between natural and our laboratory

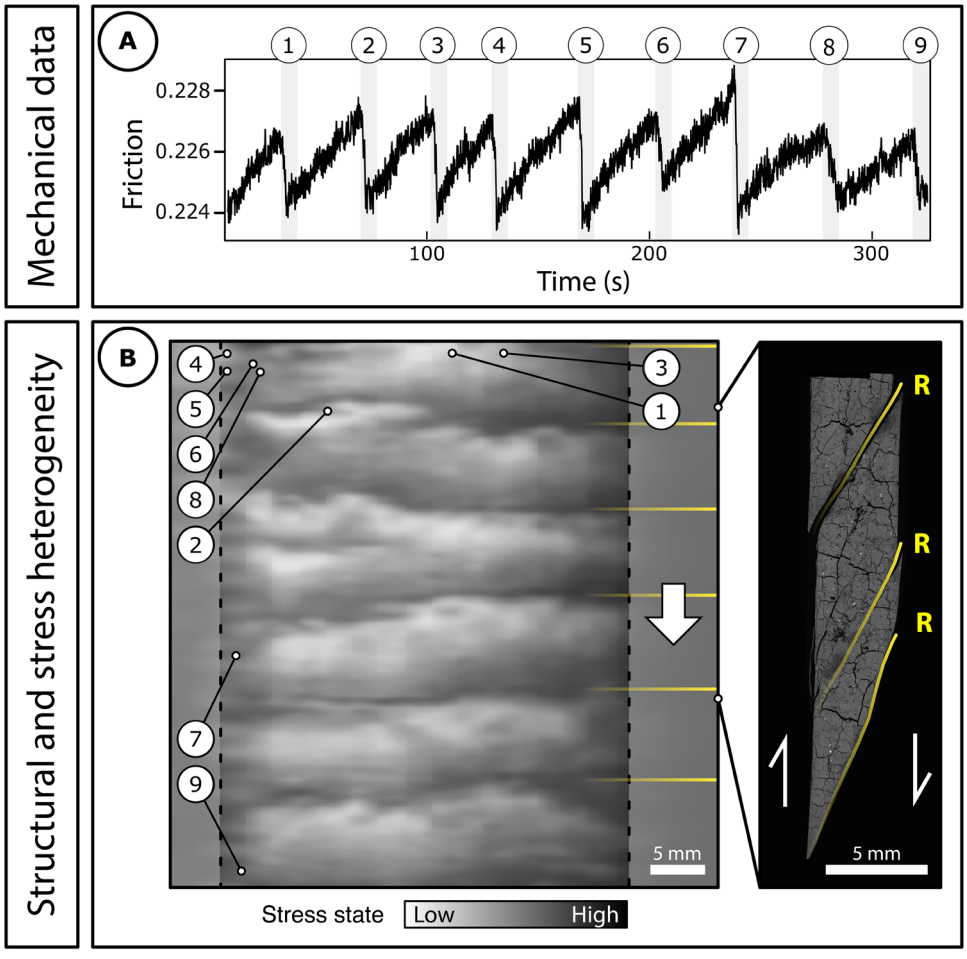

Fig. 4. The role of stress and structural heterogeneities in SSE rupture nucleation. (**A**) Mechanical data showing a series of consecutive SSE. The gray bar for each SSE represents the time window of movies S1 to S18—two movies for each slip event from 1 to 9. (**B**) Distribution of the relative state of stress along the fault surface during the SSE sequence reported in (A) (details in fig. S6). The white circles mark the nucleation sites of each SSE event. The yellow lines show the intersection between the fault surface and the Riedel shears (R) acting as structural heterogeneities. SEM image of the fault microstructure showing the cross section of the experimental fault with the Riedel shears (R) highlighted in yellow. Data of experiment b1296 (table S1).

observation support the applicability of our findings to tectonic faults, particularly to shallow subduction zones. Along these, the absence of regular seismicity is related to the abundance of clay-rich rocks (*5*, *19*, *20*). These rocks exhibit low friction, low healing rates, and rate-strengthening behavior (*17*, *22*, *24*), which hinder earthquake nucleation, therefore promoting low seismic coupling and aseismic deformation (*5*, *8*). However, shallow subduction zones also host shallow SSE (*8*, *16*) and tsunami earthquakes [(*3*, *6*, *9*–*12*); Fig. 5A]. To explain the nucleation of these peculiar seismic phenomena within rate-strengthening and weakly coupled faults, structural and frictional heterogeneities have been suggested to favor the development of unstable and coupled fault patches (*3*, *8*, *51*), whereas the transitional frictional behavior at low stresses and velocity has been proposed as a potential nucleation mechanism (*8*, *27*, *52*). Our results indicate that a relatively unexplored yet fundamental control on shallow SSE is exerted by fault fabric, stress heterogeneities, and alternative frictional mechanisms. Our experimental clay-rich faults (Fig. 5B) exhibit bulk frictional rheology with low frictional strength, null healing rate, and rate-strengthening behavior, therefore explaining the low interseismic coupling and aseismic creep often observed along the clay-rich shallow subduction zones (Fig. 5C). However, slip localization on weak faults, as documented for the 2011 Tohoku-Oki earthquake (*53*), enhances the development of frictional instabilities resulting in SSE with slow rupture velocities (Fig. 5, B and D). Our results support recent findings suggesting a key role of frictionally weak clay-rich rocks in the nucleation of shallow SSE (*17*, *27*) and suggest an alternative interpretation for the origin of shallow slow earthquakes. Furthermore, our findings offer a further perspective on the seismogenic potential of the shallowest and weakly coupled subduction interfaces with important implication for seismic and tsunami hazard.

MATERIALS AND METHODS

Experimental apparatus and procedures

Montmorillonite powder (details in fig. S1) was tested with BRAVA, a servo-controlled biaxial testing apparatus (*54*) hosted at the HP-HT laboratory of the Istituto Nazionale di Geofisica e Vulcanologia of Rome. We used the DDS configuration consisting of three steel forcing blocks squeezing two identical layers of rock powder (gouge) with initial thickness of 4 mm (Fig. 6A). The normal stress (σ_N) is

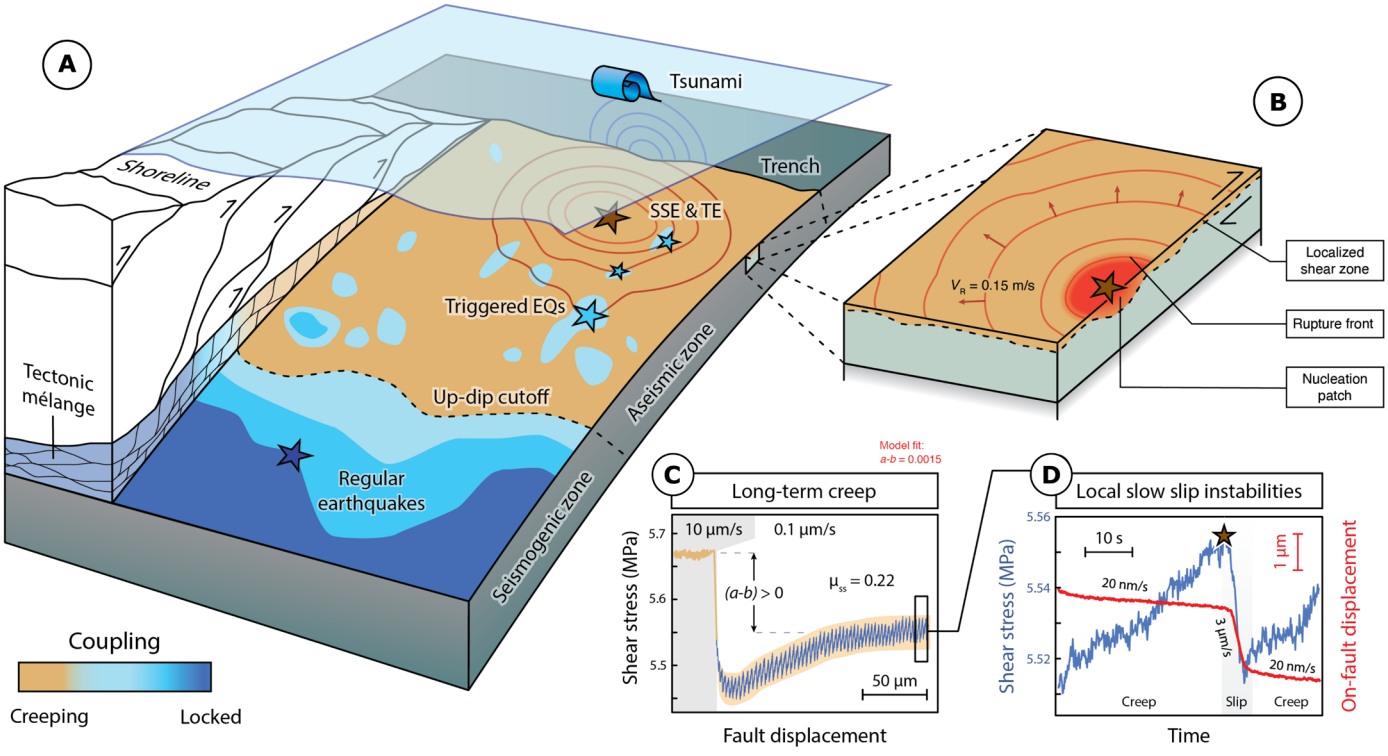

Fig. 5. Integration between structural and frictional properties. (**A**) Block diagram showing structural and frictional properties of shallow subduction zones where shallow slow-slip events (SSE) and tsunami earthquakes (TE) occur. The color bar shows the coupling degree along the subduction interface. (**B**) Model of the experimental fault at forcing velocity of 0.1 µm/s where instabilities occur. (**C**) Shear stress evolution during a velocity step displaying rate-strengthening behavior (brown) with small instabilities (blue). (**D**) Details of a laboratory SSE. Note: During interseismic phase, the fault is not locked but it is continuously creeping at nm/s. These features support the observed spectrum of fault slip behavior at shallow subduction megathrusts where aseismic creep coexists with SSE and tsunami earthquakes.

applied perpendicular to the gouge layers with a horizontal servo-controlled hydraulic piston (*54*). A vertical piston is used to apply the shear stress (τ) through the central block (slider), forcing shear deformation within the gouge layers (*54*). The force applied by the pistons is measured via strain-gauged load cells with an accuracy of ±0.03 kN (*54*). The load is converted to stress by dividing it by the area of contact within the forcing blocks (50 by 50 mm). Load point displacements are measured via linear variable displacement transformers (LVDTs) with an accuracy of ±0.01 µm. The elastic response of the pistons is linear for the stresses applied during these experiments. To obtain dynamic instabilities in the material, we reduced the stiffness of the loading system (2.96 MPa/mm) by using an acrylic block (spring) to apply the shear stress to the central slider. This procedure is widely used in literature for the study of frictional instabilities (*55*, *56*).

The experimental procedure consists of five sequential stages listed below:

1) Loading. The normal stress is applied gradually to the sample to the target value (5, 12.5, 25, 50, and 100 MPa).

2) Relaxation. Once the target normal stress is reached, the gouge layers are allowed to compact to attain an almost steady-state thickness (~15 min).

3) Run in. After compaction, the sample is sheared for a total displacement of 5 mm at a load point velocity of 10 µm/s. This stage allows the fault to reach a steady-state frictional strength and fabric (Fig. 6B).

4) Velocity step test. The experimental fault is sheared at increasing forcing velocity: 1, 3, 10, 30, 100, and 300 µm/s, for 500 µm of displacement in each step (Fig. 6C).

5) Slide-hold-slide test. This test consists of alternating sliding (displacement of 250 µm) at constant forcing velocity of 0.1 µm/s and stopping (imposing 0 velocity) at increasing hold times: 30, 100, 300, and 1000 s (Fig. 6, D and E).

All experiments were performed at 100% room-humidity conditions, and the samples were let humidifying overnight before the start of the experiment. We also performed several other frictional experiments with slightly different experimental procedure, aimed to characterize specific properties of the gouge (table S2).

Frictional properties analysis

We characterized the steady-state frictional strength (µ), the velocity dependence of friction (*a*-*b*), and the healing behavior (β). We used the rate and state friction theory (RSF) (*30*–*32*) as framework for our analysis. The friction coefficient, µ, is retrieved as the linear constant of proportionality between steady-state shear stress and normal stress, using Eq. 1

$$\tau = \mu\sigma_n + c \quad (1)$$

where *c* is the cohesion term, which can be assumed negligible. During the velocity step tests, the forcing velocity is varied from V_0 to V, which causes a variation of frictional strength characterized by a direct and evolution effect (Fig. 6, C and D). The direct

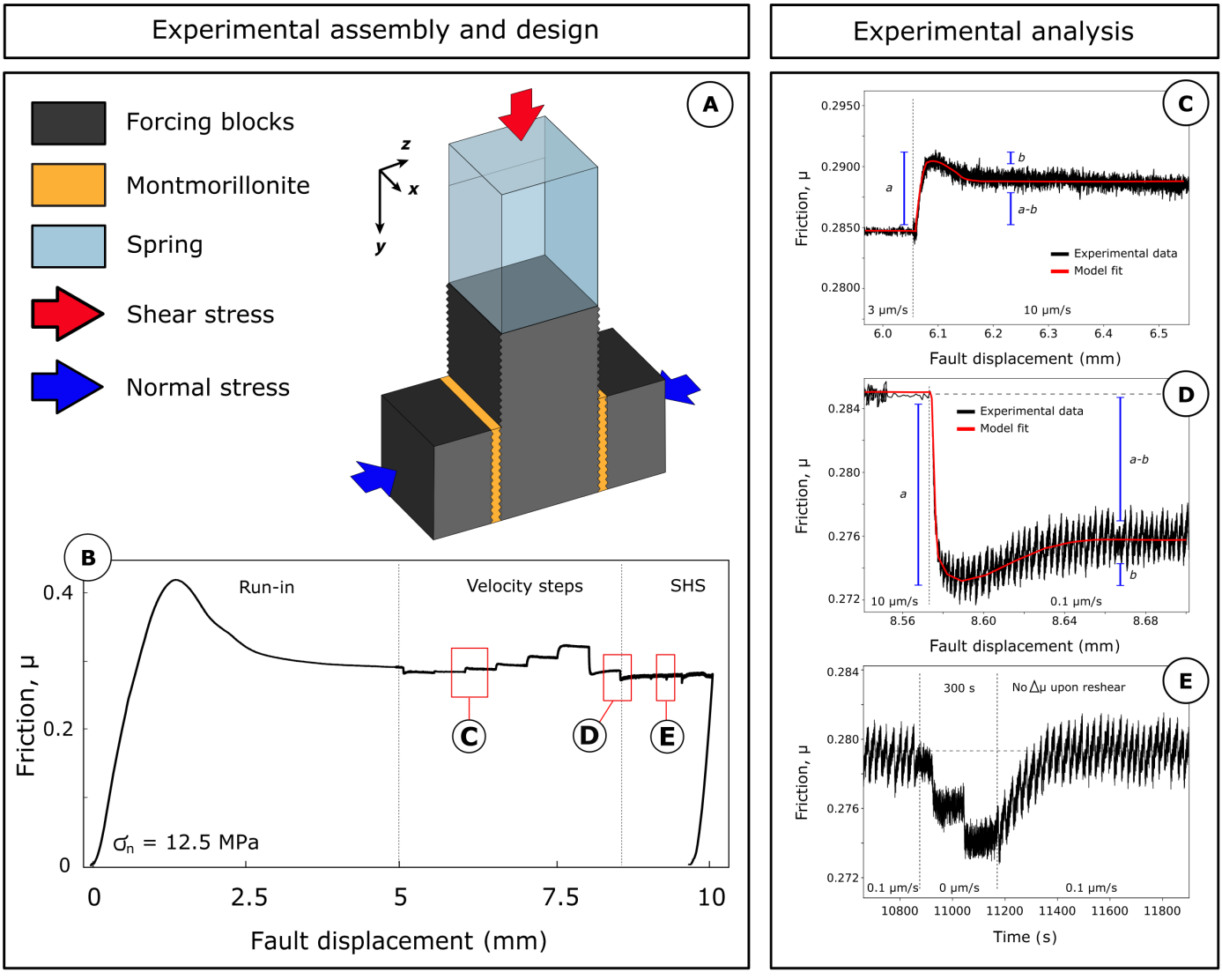

Fig. 6. Experimental design and frictional analysis. (**A**) Detail of the double direct shear assembly. (**B**) Evolution of friction as a function of shear displacement for one experiment (b1118). Our procedure consisted of a run-in phase followed by velocity step tests and slide-hold-slide (SHS) test. (**C** and **D**) Detail of a velocity step tests from 3 to 10 μm/s and from 10 to 0.1 μm/s, respectively. Black lines represent the experimental data, and red lines represent the best-fit model using RSF. (**E**) Detail of a 300-s slide-hold-slide test showing evolution of friction with hold time and re-shear. Note that in (D) and (E), the stick-slip behavior is superimposed on a trend that can be modeled using RSF.

effect scales with $a \log_e(V/V_0)$, where a is an empirical parameter (*30*, *31*). The subsequent evolution of friction to a successive steady state scales with $b \log_e(V/V_0)$, where b is also an empirical parameter (*30*, *31*). The (a-b) parameter defines the velocity dependence of friction:

$$(a-b) = \Delta\mu_{ss} / \log_e(V/V_0) \quad (2)$$

where $\Delta\mu_{ss}$ is the difference between the dynamic steady-state frictional strength after and before the step in shearing velocity from V_0 to V (*30*, *31*). Negative values of (a-b) define a velocity-weakening behavior, which is a required condition for frictional instability (*32*, *40*). Positive values of (a-b) define a velocity-strengthening behavior, suggesting aseismic creep. Each velocity step was inverted using RSF equations (Eq. 3) coupled with the Dieterich law (Eq. 4), an evolution law that defines the state variable θ (*29*):

$$\mu = \mu_0 + a \log_e(V/V_0) + b \log_e(V_0\theta/D_c) \quad (3)$$

$$d\theta/dt = 1 - \theta V/D_c \quad (4)$$

where μ_0 is steady-state frictional strength at slip velocity V_0 and D_c is the critical slip distance (*30*, *31*). To model velocity steps, Eqs. 3 and 4 are coupled with Eq. 5, which defines the elastic coupling between the sliding surface and the loading medium:

$$d\mu/dt = k(V_f - V) \quad (5)$$

where V_f is the forcing velocity (the one applied by the vertical piston) and k is the loading system stiffness normalized by normal stress. These equations are solved simultaneously using a fifth-order Runge-Kutta integration. a, b, and D_c were retrieved, for each velocity step, as best fit

values using a least-squares iterative method to solve the inverse nonlinear problem (*22*, *57*). During slide-hold-slide test, the frictional healing ($\Delta\mu$) was obtained as the difference between the friction peak measured during re-shear following each hold and the steady-state friction before the hold [(*32*); Fig. 6E]. Frictional healing rate (β) was retrieved as the linear variation of $\Delta\mu$ with logarithm of the hold time (t_h).

$$\beta = \Delta\mu / \log_{10}(\Delta t_h) \quad (6)$$

Microstructural analysis

At the end of each experiment, we carefully extracted the deformed samples to preserve the entire gouge thickness, comprised within the forcing blocks (*58*). After extraction, we carefully embedded the samples in epoxy resin (Struers EpoFix) at room pressure. Once the resin was hardened, we cut the samples perpendicular to the shear plane and parallel to the sense of shear to expose the kinematic section of the microstructure (*59*). The cut surfaces were polished with increasingly finer sandpaper, grit of 600–2000, and then by finer diamond paste, 6–1 μm (*57*). All lapping steps were performed at low velocity and lubricated with oil-based fluids to avoid water-enhanced erosion of the samples. Polished surfaces were coated with graphite for the microstructural analysis, which was conducted with a field-emission scanning electron microscope (SEM) hosted at the Istituto Nazionale di Geofisica e Vulcanologia of Rome. Imagery was collected in backscattered mode.

Experimental design for direct video documentation

To allow direct optical documentation of the fault surface, we used the same experimental procedure described above but using a slightly modified sample assembly. We replaced the central slider with a transparent acrylic forcing block (applying shear stress). Differently from the metal slider, the acrylic block has a nominally flat surface in contact with the sample (compare Figs. 6A and 7A). We also replaced the lateral forcing blocks with nominally flat surfaces to match the central slider. The coupling between the gouge and the forcing blocks is high enough to force deformation to occur within the gouge and not at the interface. This is confirmed by mechanical data showing the same frictional properties [μ, (a-b), β; fig. S4] and fault slip behavior (i.e., instabilities, stress drop, and recurrence time; fig. S4) for experiments with standard DDS configuration and with acrylic central block. In other words, the acrylic central block alters neither the bulk mechanical behavior nor the stick-slip instabilities and experimental microstructures are the same (fig. S4). A further test has been performed with intermediate roughness of the forcing blocks, obtaining the same results. This indicates a negligible influence of the forcing block roughness in the mechanical data.

High-resolution imaging of the fault surface was performed with a NAC Memrecam HX-3 high-speed camera operating at 500 frames per second (500 Hz), with a resolution of 192 (horizontal) by 600 (vertical) pixels, and a pixel pitch of 0.0833 mm/pixel [>300 pixels per inch (ppi)]. The experimental setup is depicted in Fig. 7. The camera is positioned with a line of sight tilted by 45° from the fault surface and perpendicular to the sliding direction. The fault surface is illuminated with a homogeneous source of white light placed at the other side of the central transparent sliding block. This experimental set allows the camera to record changes of reflectivity along the surface. Changes in reflectivity (imaged as variation in

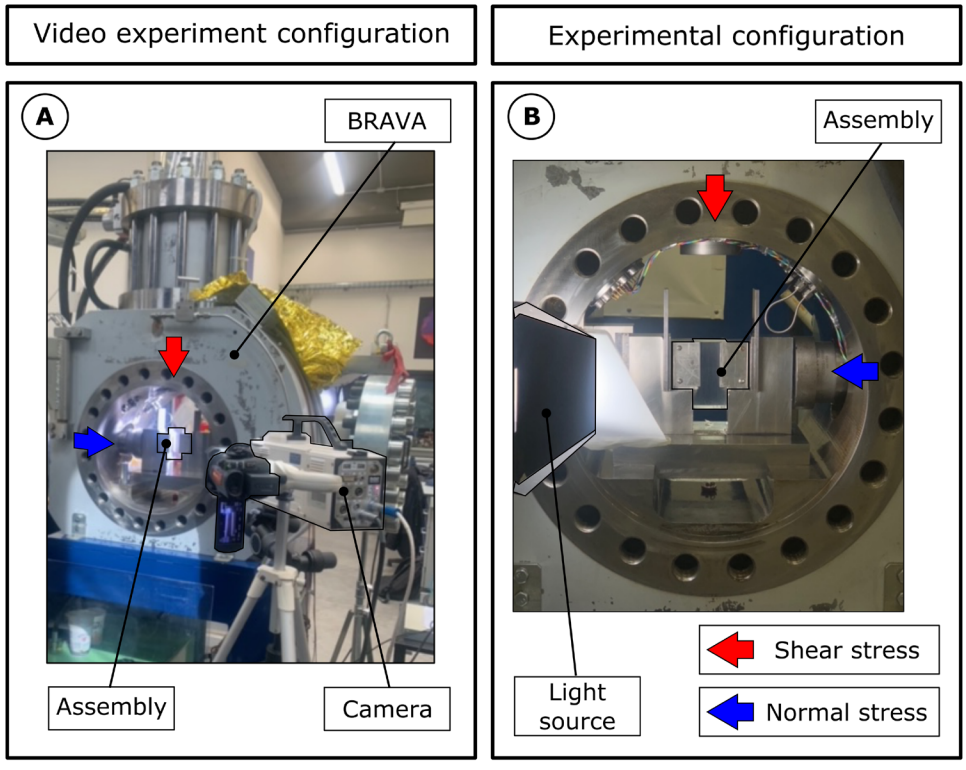

Fig. 7. Configuration of the video experiment. (**A**) Experimental configuration for the video experiments set on BRAVA apparatus. (**B**) Close-up of the assembly for the video experiment with the highlighted light-source setup (see Fig. 2A for further details).

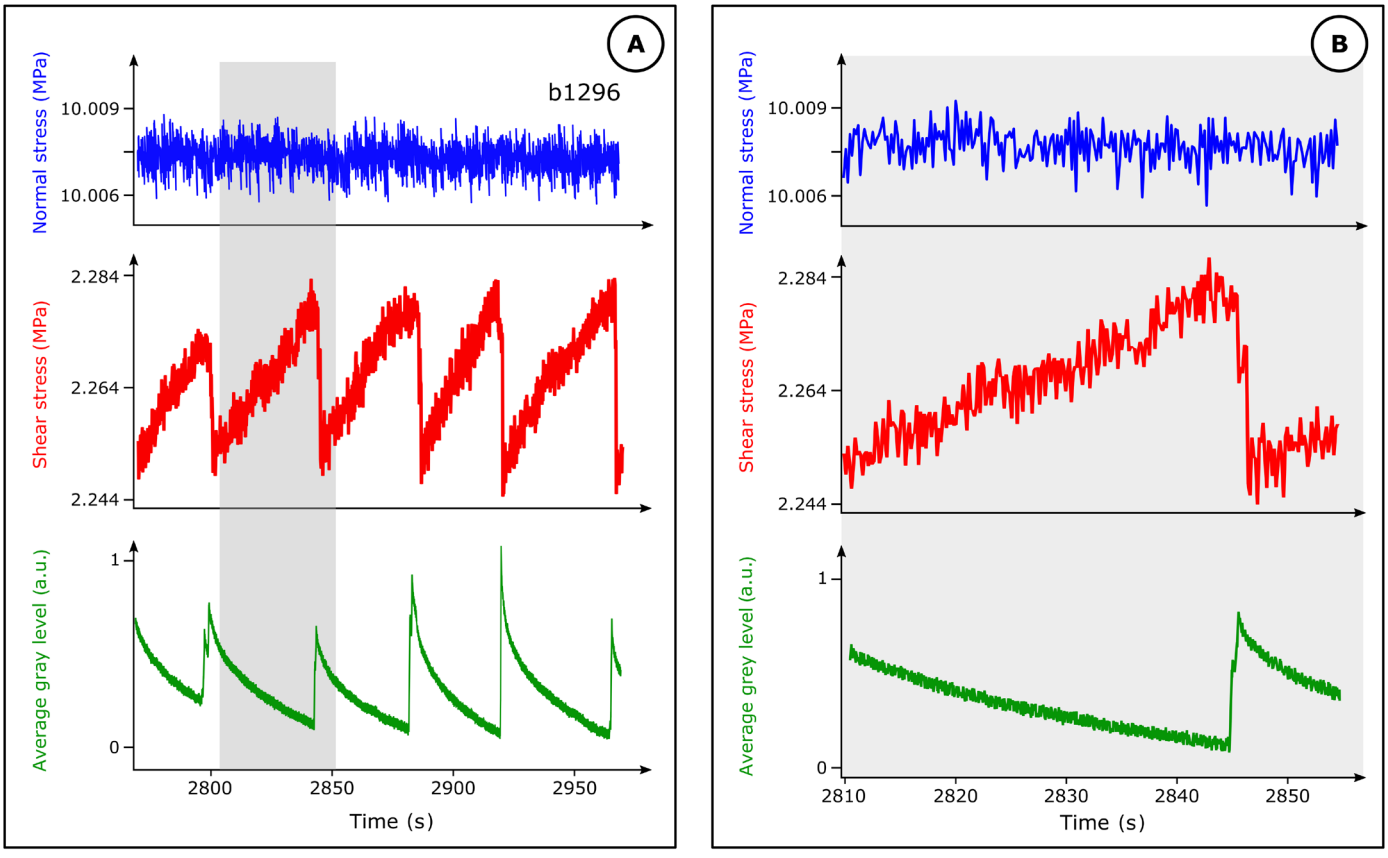

Fig. 8. Comparison between mechanical data and reflectivity changes quantified in average gray level. (**A**) Evolution of normal stress (blue), shear stress (red), and reflectivity (green) during a series of consecutive stick-slip events. (**B**) Evolution of normal stress, shear stress, and reflectivity in a single stick-slip cycle [gray bar in (A)].

gray level) correspond to changes of the local state of stress projected on the fault surface (Fig. 8).

Digital image analysis

Image processing has been performed on the footage using both static and rolling background removal. In the static background removal, a background image was calculated as the pixel-wise average of the 500 frames preceding the beginning of the portion of interest of the video, which corresponds to the final part of the interseismic time and represents the initial state of stress on the fault surface. The background image was then subtracted from each of the subsequent frames. The resulting video displays changes in the gray level (quantified in a.u.) relative to the background image (Fig. 3A and movies S10 to S18). From the static background removal video of a transient slip event (movie S1), we projected the average gray level along the *y* axis and analyzed the variation in time, obtaining the videogram of Fig. 3B. The same procedure is used at discrete times to build the variation of gray level of Fig. 3C. The average gray level has been calculated after Gaussian filtering of the original images by averaging *x*-wise over the visible fault surface (Fig. 3A). The rolling background removal consists, for each frame, of the subtraction of a previous frame with an arbitrary separation of time. The optimal separation for visualization has been selected by trial and error at five time frames. The resulting image has been normalized over a narrow range of gray levels to enhance contrast. The rolling background reveals the portion of the fault in which stress changes have occurred between five time frames, allowing to trace and visualize the position of the rupture front (movies S1 to S9). Selected time frames were stacked to compose image Fig. 3A, which shows in light gray the position of the wrinkle-like pulse.

Derivation of the change in the state of stress on fault

The evolution of the state of stress along the fault surface has been tracked by synchronizing and correlating the stress measured by the load cell of the BRAVA apparatus (*54*) with changes in the reflectivity of the fault surface detected via digital image analysis and quantified in gray level (a.u.). We observed that the bulk fault reflectivity (i.e., average gray level) changes simultaneously with the variation of the stresses acting on fault as measured by the load cells (i.e., during stick-slip cycles; Fig. 8A). Our data also show that the average gray level (i.e., bulk fault reflectivity) has an inverse and nonlinear relation with stress: Reflectivity increases as the stress decreases and vice versa (Fig. 8B).

Supplementary Materials

This PDF file includes:

Figs. S1 to S7
Tables S1 and S2
Legends for movies S1 to S18

Other Supplementary Material for this manuscript includes the following:

Movies S1 to S18

REFERENCES AND NOTES

1. S. Ide, G. C. Beroza, D. R. Shelly, T. Uchide, A scaling law for slow earthquakes. *Nature* **447**, 76–79 (2007).
2. Z. Peng, J. Gomberg, An integrated perspective of the continuum between earthquakes and slow-slip phenomena. *Nat. Geosci.* **3**, 599–607 (2010).
3. T. Lay, H. Kanamori, C. J. Ammon, K. D. Koper, A. R. Hutko, L. Ye, H. Yue, T. M. Rushing, Depth-varying rupture properties of subduction zone megathrust faults. *J. Geophys. Res. Solid Earth* **117**, 9133 (2012).
4. R. Bürgmann, The geophysics, geology and mechanics of slow fault slip. *Earth Planet. Sci. Lett.* **495**, 112–134 (2018).
5. C. H. Scholz, *The Mechanics of Earthquakes and Faulting* (Cambridge Univ. Press, 2018).
6. J. Polet, H. Kanamori, Shallow subduction zone earthquakes and their tsunamigenic potential. *Geophys. J. Int.* **142**, 684–702 (2000).
7. G. Rogers, H. Dragert, Episodic tremor and slip on the Cascadia subduction zone: The chatter of silent slip. *Science* **300**, 1942–1943 (2003).
8. D. M. Saffer, L. M. Wallace, The frictional, hydrologic, metamorphic and thermal habitat of shallow slow earthquakes. *Nat. Geosci.* **8**, 594–600 (2015).
9. H. Kanamori, Mechanism of tsunami earthquakes. *Phys. Earth Planet. In.* **6**, 346–359 (1972).
10. H. Kanamori, M. Kikuchi, The 1992 Nicaragua earthquake: A slow tsunami earthquake associated with subducted sediments. *Nature* **361**, 714–716 (1993).
11. S. L. Bilek, T. Lay, Tsunami earthquakes possibly widespread manifestations of frictional conditional stability. *Geophys. Res. Lett.* **29**, 18-1–18-4 (2002).
12. Lay, The surge of great earthquakes from 2004 to 2014. *Earth Planet. Sci. Lett.* **409**, 133–146 (2015).
13. R. Bell, C. Holden, W. Power, X. Wang, G. Downes, Hikurangi margin tsunami earthquake generated by slow seismic rupture over a subducted seamount. *Earth Planet. Sci. Lett.* **397**, 1–9 (2014).
14. S. L. Bilek, E. R. Engdahl, Rupture characterization and aftershock relocations for the 1994 and 2006 tsunami earthquakes in the Java subduction zone. *Geophys. Res. Lett.* **34**, 31357 (2007).
15. H. Noda, N. Lapusta, Stable creeping fault segments can become destructive as a result of dynamic weakening. *Nature* **493**, 518–521 (2013).
16. Wallace, Slow slip events in New Zealand. *Annu. Rev. Earth Planet. Sci.* **48**, 175–203 (2020).
17. S. Shreedharan, D. Saffer, L. M. Wallace, C. Williams, Ultralow frictional healing explains recurring slow slip events. *Science* **379**, 712–717 (2023).
18. J.-P. Avouac, From geodetic imaging of seismic and aseismic fault slip to dynamic modeling of the seismic cycle. *Annu. Rev. Earth Planet. Sci.* **43**, 233–271 (2015).
19. Vrolijk, On the mechanical role of smectite in subduction zones. *Geology* **18**, 703–707 (1990).
20. R. Von Huene, D. W. Scholl, Observations at convergent margins concerning sediment subduction, subduction erosion, and the growth of continental crust. *Rev. Geophys.* **29**, 279–316 (1991).
21. Ito, Obara, Very low frequency earthquakes within accretionary prisms are very low stress-drop earthquakes. *Geophys. Res. Lett.* **33**, 25883 (2006).
22. D. M. Saffer, C. Marone, Comparison of smectite-and illite-rich gouge frictional properties: Application to the updip limit of the seismogenic zone along subduction megathrusts. *Earth Planet. Sci. Lett.* **215**, 219–235 (2003).
23. M. J. Ikari, C. Marone, D. M. Saffer, On the relation between fault strength and frictional stability. *Geology* **39**, 83–86 (2011).
24. M. J. Ikari, D. M. Saffer, Comparison of frictional strength and velocity dependence between fault zones in the Nankai accretionary complex. *Geochem. Geophys. Geosyst.* **12**, 3442 (2011).
25. S. A. M. Den Hartog, A. R. Niemeijer, C. J. Spiers, Friction on subduction megathrust faults: Beyond the illite–muscovite transition. *Earth Planet. Sci. Lett.* **373**, 8–19 (2013).
26. A. S. Okamoto, A. R. Niemeijer, T. Takeshita, B. A. Verberne, C. J. Spiers, Frictional properties of actinolite-chlorite gouge at hydrothermal conditions. *Tectonophysics* **779**, 228377 (2020).
27. M. J. Ikari, A. J. Kopf, Seismic potential of weak, near-surface faults revealed at plate tectonic slip rates. *Sci. Adv.* **3**, e1701269 (2017).
28. Y. Yang, E. M. Dunham, Effect of porosity and permeability evolution on injection-induced aseismic slip. *J. Geophys. Res. Solid Earth* **126**, e2020JB021258 (2021).
29. A. Perez-Silva, Y. Kaneko, M. Savage, L. Wallace, E. Warren-Smith, Characteristics of slow slip events explained by rate-strengthening faults subject to periodic pore fluid pressure changes. *J. Geophys. Res. Solid Earth* **128**, e2022JB026332 (2023).
30. J. H. Dieterich, Modeling of rock friction: 1. Experimental results and constitutive equations. *J. Geophys. Res. Solid Earth* **84**, 2161–2168 (1979).
31. A. Ruina, Slip instability and state variable friction laws. *J. Geophys. Res. Solid Earth* **88**, 10359–10370 (1983).
32. C. Marone, Laboratory-derived friction laws and their application to seismic faulting. *Annu. Rev. Earth Planet. Sci.* **26**, 643–696 (1998).
33. S. . Nielsen, J. Taddeucci, S. Vinciguerra, Experimental observation of stick-slip instability fronts. *Geophys. J. Int.* **180**, 697–702 (2010).
34. Y. Kaneko, S. B. Nielsen, B. M. Carpenter, The onset of laboratory earthquakes explained by nucleating rupture on a rate-and-state fault. *J. Geophys. Res. Solid Earth* **121**, 6071–6091 (2016).
35. H. Shlomai, J. Fineberg, The structure of slip-pulses and supershear ruptures driving slip in bimaterial friction. *Nat. Commun.* **7**, 11787 (2016).
36. A. Gounon, S. Latour, J. Letort, S. El Arem, Rupture nucleation on a periodically heterogeneous interface. *Geophys. Res. Lett.* **49**, e2021GL096816 (2022).
37. V. Rubino, N. Lapusta, A. J. Rosakis, Intermittent lab earthquakes in dynamically weakening fault gouge. *Nature* **606**, 922–929 (2022).
38. S. B. L. Cebry, C. Y. Ke, S. Shreedharan, C. Marone, D. S. Kammer, G. C. McLaskey, Creep fronts and complexity in laboratory earthquake sequences illuminate delayed earthquake triggering. *Nat. Commun.* **13**, 6839 (2022).
39. W. Steinhardt, S. Dillavou, M. Agajanian, S. M. Rubinstein, E. E. Brodsky, Seismological stress drops for confined ruptures are invariant to normal stress. *Geophys. Res. Lett.* **50**, e2022GL101366 (2023).
40. J. H. Dieterich, B. D. Kilgore, Direct observation of frictional contacts: New insights for state-dependent properties. *Pure Appl. Geophys.* **143**, 283–302 (1994).
41. K. Viswanathan, N. K. Sundaram, Distinct stick-slip modes in adhesive polymer interfaces. *Wear* **376**–**377**, 1271–1278 (2017).
42. M. Cocco, S. Aretusini, C. Cornelio, S. B. Nielsen, E. Spagnuolo, E. Tinti, G. Di Toro, Fracture energy and breakdown work during earthquakes. *Annu. Rev. Earth Planet. Sci.* **51**, 217–252 (2023).
43. D. J. Andrews, Y. Ben-Zion, Wrinkle-like slip pulse on a fault between different materials. *J. Geophys. Res. Solid Earth* **102**, 553–571 (1997).
44. G. Lykotrafitis, A. J. Rosakis, G. Ravichandran, Self-healing pulse-like shear ruptures in the laboratory. *Science* **313**, 1765–1768 (2006).
45. V. Lambert, N. Lapusta, S. Perry, Propagation of large earthquakes as self-healing pulses or mild cracks. *Nature* **591**, 252–258 (2021).
46. A. Schallamach, How does rubber slide? *Wear* **17**, 301–312 (1971).
47. D. M. Saffer, K. M. Frye, C. Marone, K. Mair, Laboratory results indicating complex and potentially unstable frictional behavior of smectite clay. *Geophys. Res. Lett.* **28**, 2297–2300 (2001).
48. F. X. Passelègue, A. Schubnel, S. Nielsen, H. S. Bhat, R. Madariaga, From sub-Rayleigh to supershear ruptures during stick-slip experiments on crustal rocks. *Science* **340**, 1208–1211 (2013).
49. G. C. . Mclaskey, F. Yamashita, Slow and fast ruptures on a laboratory fault controlled by loading characteristics. *J. Geophys. Res. Solid Earth* **122**, 3719–3738 (2017).
50. S. Xu, E. Fukuyama, F. Yamashita, H. Kawakata, K. Mizoguchi, S. Takizawa, Fault strength and rupture process controlled by fault surface topography. *Nat. Geosci.* **16**, 94–100 (2023).
51. K. Wang, S. L. Bilek, Invited review paper: Fault creep caused by subduction of rough seafloor relief. *Tectonophysics* **610**, 1–24 (2014).
52. K. Im, D. Saffer, C. Marone, J. P. Avouac, Slip-rate-dependent friction as a universal mechanism for slow slip events. *Nat. Geosci.* **13**, 705–710 (2020).
53. K. . Wang, M. Kinoshita, Dangers of being thin and weak. *Science* **342**, 1178–1180 (2013).
54. C. Collettini, G. Di Stefano, B. Carpenter, P. Scarlato, T. Tesei, S. Mollo, F. Trippetta, C. Marone, G. Romeo, L. Chiaraluce, A novel and versatile apparatus for brittle rock deformation. *Int. J. Rock Mech. Min. Sci.* **66**, 114–123 (2014).
55. M. M. Scuderi, C. Marone, E. Tinti, G. Di Stefano, C. Collettini, Precursory changes in seismic velocity for the spectrum of earthquake failure modes. *Nat. Geosci.* **9**, 695–700 (2016).
56. J. R. Leeman, C. Marone, D. M. Saffer, Frictional mechanics of slow earthquakes. *J. Geophys. Res. Solid Earth* **123**, 7931–7949 (2018).
57. M. L. Blanpied, C. J. Marone, D. A. Lockner, J. D. Byerlee, D. P. King, Quantitative measure of the variation in fault rheology due to fluid-rock interactions. *J. Geophys. Res. Solid Earth* **103**, 9691–9712 (1998).
58. G. Volpe, G. Pozzi, C. Collettini, Y-B-P-R or S-C-C′? Suggestion for the nomenclature of experimental brittle fault fabric in phyllosilicate-granular mixtures. *J. Struct. Geol.* **165**, 104743 (2022).
59. C. W. Passchier, A Mohr circle construction to plot the stretch history of material lines. *J. Struct. Geol.* **12**, 513–515 (1990).

Acknowledgments: We thank D. Mannetta for his help with thin section preparation and M. Nazzari for the support at the SEM-INGV laboratory. We also thank M. M. Scuderi, E. Tinti, and M. Cocco for fruitful discussion. **Funding:** This work was supported by ERC grant Nr. 259256 GLASS (to C.C.), ERC grant Nr. 835012 TECTONIC (to C.M.), and ERC grant FEAR 856559

(to G.P.). **Author contributions:** Conceptualization: G.V. and G.P. Data curation: G.V., J.T., and G.P. Formal analysis: G.V., J.T., and G.P. Investigation: G.V., J.T., and G.P. Methodology: G.V., J.T., and G.P. Writing—original draft: G.V., C.C., and G.P. Writing—review and editing: G.V., C.M., G.P., and J.T. Resources: G.V., J.T., C.M., and G.P. Funding acquisition: C.C. and C.M. Validation: G.V., C.C., C.M., and G.P. Supervision: G.V., C.C., C.M., and G.P. Visualization: G.V., J.T., and G.P. Software: G.V., G.P., and J.T. Project administration: G.V., C.C., C.M., and G.P. **Competing interests:** The authors declare that they have no competing interests. **Data and materials availability:** All data needed to evaluate the conclusions in the paper are present in the paper and/or the Supplementary Materials.

Submitted 21 November 2023
Accepted 23 May 2024
Published 28 June 2024
10.1126/sciadv.adn0869